

# Performance evaluation of a vortex generator heat transfer surface and comparison with different high performance surfaces

U. BROCKMEIER,† TH. GUENTERMANN‡ and M. FIEBIGER‡

† Institut für Energietechnik and ‡ Institut für Thermo- und Fluidodynamik,  
Ruhr-Universität Bochum, FRG

(Received 19 February 1992 and in final form 12 November 1992)

**Abstract**—A comparative assessment of five different heat transfer configurations for operation in compact heat exchangers is presented. The configurations under consideration are four standard heat exchanger surfaces—two plain fin, an offset strip and a louvered fin geometry—and one surface with so called vortex generators for heat transfer augmentation. In the case of the standard surfaces, the basic performance characteristics in the form of heat transfer and friction data versus the Reynolds number have been taken from published experimental results. In the case of the vortex generator surface, the performance characteristics have been derived from a numerical prediction of the flow and temperature field in a closely spaced parallel plate channel with vortex generators in the form of delta wings mounted on the channel walls. In comparison to the plain fin surface with a rectangular cross section, the vortex generator surface shows best performance characteristics allowing a reduction in heat transfer surface area of 76%, for fixed heat duty and for fixed pumping power.

## INTRODUCTION

THE NEED for high performance heat exchanger devices for operation in small-size and lightweight heat exchangers (cooling systems in automobiles and spacecrafts), high heat duty exchangers in power plants (aircooled condensers, nuclear fuel rods), and numerous other applications has resulted in the development of various designs of heat transfer surfaces. Objectives of optimization are, besides others, the capital and operating costs. Both can be positively affected by either increasing the heat transfer coefficient or increasing the effective heat transfer surface area per volume, or both. In most cases, one of these three basic methods is employed in enhanced surface geometries [1]. Among current heat exchangers, different basic flow geometry classes can be distinguished, i.e. internal flows in tubes, external flows normal and axial to tubes (rod bundles) and channel flows in closely spaced parallel plate channels. The latter ones belong to the class under consideration here. Five different types of plate channel heat exchangers, each showing the typical plate fin surface for gases, are investigated. Due to their small hydraulic diameters and the low density of gaseous fluids, the surfaces are usually operated in the Reynolds number range  $500 \leq Re \leq 1500$  [1]. The five types under consideration are:

- *Type A*: Plain fin exchanger surface with fins forming a flow channel with rectangular cross sections (see Fig. 1 and for details Fig. A1 in the Appendix). The enhancement is mainly achieved by an increase in the effective heat transfer surface area per volume.

- *Type B*: Plain fin exchanger surface with fins forming a flow channel with triangular cross sections (see Fig. 1 and for details Fig. A2 in the Appendix). As in the case of Type A, the enhancement is mainly achieved by an increase in surface area density.
- *Type C*: Offset strip fin exchanger surface (see Fig. 1 and for details Fig. A3 in the Appendix). The enhancement is achieved by both an increase in the effective surface area and in the heat transfer coefficient due to repeatedly developing boundary layers on the short strips.
- *Type D*: Louvered fin exchanger surface (see Fig. 1 and for details Fig. A4 in the Appendix). Similar to Type C, the enhancement is achieved by an increase of effective surface area and in the heat transfer coefficient. Rather than offsetting the slit strips, the entire surfaces are louvered.
- *Type E*: Vortex generator surface (see Fig. 1 and for details Fig. A5 in the Appendix). The enhancement is mainly achieved by an increase in heat transfer due to longitudinally spiraling vortices exchanging fluid from wall to core regions of the flow.

To obtain a basis for a comparative assessment of different surface types, an object of the optimization has to be defined. Due to its commercial relevance, the reduction of capital costs by means of a reduction of necessary heat transfer surface area for constant heat duty and pressure loss has been chosen to serve as object of optimization. Calculation and comparison of the performance objective—reduced surface area—requires algebraic relations which quantify the objective function (e.g. necessary surface area as

## NOMENCLATURE

$a$	coefficient equation (12) [—]	$T$	temperature [K]
$A$	total heat transfer area (primary + secondary) [m <sup>2</sup> ]	$\Delta T_m$	logarithmic mean temperature difference, equation (6) [K]
$A_c$	minimum free flow area [m <sup>2</sup> ]	$u_m$	fluid mean axial velocity through heat exchanger core, $G/\rho$ [m s <sup>-1</sup> ]
$b$	fin spacing [m]	$u$	local axial velocity [m s <sup>-1</sup> ]
$b$	coefficient, equation (13) [—]	$U_x$	wetted perimeter of the channel at position $x$ [m]
$c_f$	Fanning friction factor, equation 11 [—]	$W$	mass flow rate [kg s <sup>-1</sup> ]
$c_p$	fluid specific heat at constant pressure [J kg <sup>-1</sup> K <sup>-1</sup> ]	$x$	coordinate in main flow direction
$f$	apparent mean friction factor, equation (7) [—]	$y$	coordinate parallel to walls
$g$	function, equations (1), (2) and (21) [—]	$z$	coordinate normal to walls.
$G$	exchanger flow-stream mass velocity, $W/A_o$ [kg m <sup>-2</sup> s <sup>-1</sup> ]		
$h$	convective heat transfer coefficient [W m <sup>-2</sup> K <sup>-1</sup> ]	Greek symbols	
$H$	plate spacing [m]	$\beta$	vortex generator angle of attack [°]
$j$	Colburn heat transfer modulus, $St \cdot Pr^{2/3}$ [—]	$\epsilon$	heat exchanger effectiveness [—]
$k$	thermal conductivity [W m <sup>-1</sup> K <sup>-1</sup> ]	$\mu$	fluid dynamic viscosity coefficient [N s m <sup>-2</sup> ]
$L$	heat exchanger total length [m]	$\rho$	fluid density [kg m <sup>-3</sup> ]
$l$	heat exchanger module length [m]	$\tau_s$	shear stress [N m <sup>-2</sup> ].
$m$	exponent equation (12) [—]		
$M$	number of heat exchanger modules [—]	Subscripts	
$NTU$	number of heat transfer units, $h \cdot A/(W \cdot c_p)$ [—]	bi	bulk inlet
$Nu$	Nusselt number, $h \cdot 4r_h/k$ [—]	bo	bulk outlet
$n$	exponent equation (13) [—]	i	inlet
$P$	fluid pumping power [W]	l	value corresponding to a single module
$Pr$	Prandtl number, $\mu \cdot c_p/k$ [—]	m	mean
$\Delta p_{st}$	fluid static pressure drop [N m <sup>-2</sup> ]	o	reference surface
$Q$	heat transfer rate [W]	w	wall
$Re$	Reynolds number, $G \cdot 4r_h/\mu$ [—]	vg	vortex generator
$r_h$	hydraulic radius, $A_c \cdot L/A$ [m]	$x$	axial position
$St$	Stanton number, $Nu/(Re \cdot Pr)$ [—]	$xy$	plane, parallel to walls, equation (8)
$t$	offset strip fin length [m]	$\bar{xy}$	mean from both channel walls, equation (8).

a function of heat transfer, mass flow rate, etc.) under certain constraints (fixed heat duty, fixed pumping power, temperature differences, etc.). Basic data to enter these algebraic relations are, besides geometry data, fluid properties and operating data, the Colburn factor,  $j$ , and the friction factor,  $f$ , versus Reynolds number,  $Re$ . Consequently, it is convenient to correlate the basic heat transfer and flow friction performance data existing in tabular or graphical form from experimental or numerical investigations and to derive algebraic expressions.

In the case of the Surface Types A, B, C and D (Fig. 1), the data of  $j$  and  $f$  vs  $Re$  are based on experimental results. The data for Type E (Fig. 1) are results of a numerical prediction of the flow and temperature field in a sample geometry with details presented in this paper.

## EXPERIMENTAL AND NUMERICAL PERFORMANCE DATA

Due to a relatively poor experimental data basis for vortex generator surfaces, the performance data of the Type E surface have been computationally predicted. In order to enable their comparison to the experimental data (Types A, B, C, and D), the numerical boundary conditions had to be adapted to the experimental boundary conditions. Thus, the governing assumptions (Ass.) associated with the experimental data are discussed in the following with a view to the consequences for a numerical prediction of the Type E data.

*Experimental data*

Performance data for a large variety of different compact heat exchangers based on experimental

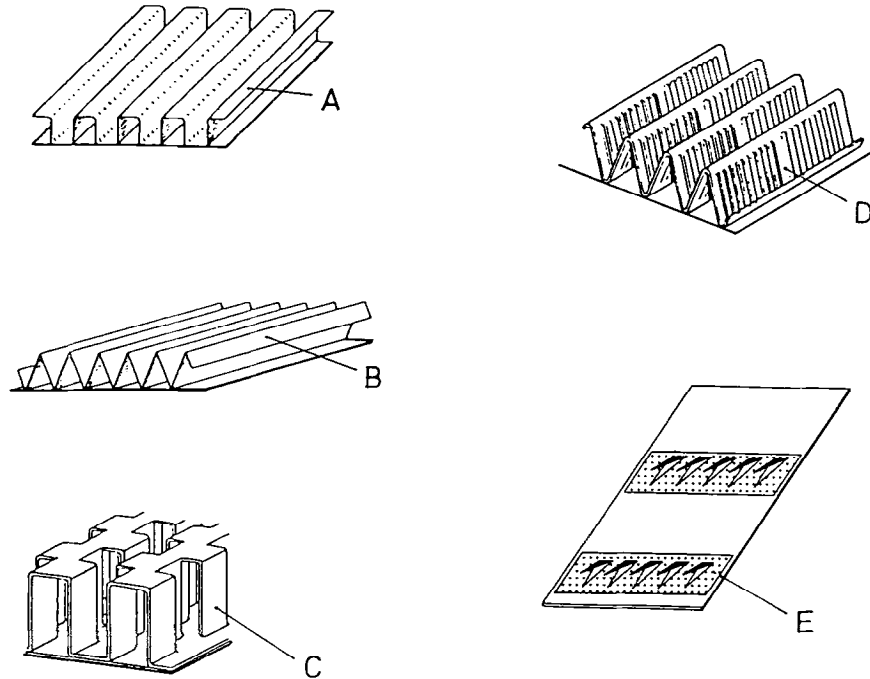


FIG. 1. Heat transfer surface types subject to the comparison. Closely spaced parallel plate channels with plain fins forming rectangular cross sections (A), and triangular cross sections (B), (C) offset strip fins, (D) louvered fins (all taken from ref. [1]) and (E) vortex generators. Detailed geometrical data are given in the Appendix.

investigations are given in ref. [2]. Among others, the basic data for the Surface Types A, B, C and D are presented in ref. [2].

The experiments were carried out in a test apparatus operating the test surfaces in cross flow with air on one side and condensing steam on the other (for a detailed description of the experimental apparatus, the measurement technique and uncertainties in the results see ref. [2]). The flow loss and heat transfer data presented in ref. [2] were corrected for effects of the pressure losses at the entrance and exit of the test section and for effects of the wall and the steam side condensate film resistance as well as the temperature ineffectiveness of the extended parts of the total transfer surface. (The basic heat transfer data given in ref. [2] are to be corrected for non unity fin efficiency  $\eta_f < 1$ , before entering a heat exchanger design procedure.)

This leads to:

*Ass. 1:* The heat transfer (and flow loss) data reflect the behavior of the fluid on only one side—the gas side—of the transfer surface, i.e. the thermal resistance on the condensing steam side and the wall resistance are assumed to be zero. In addition, the fins are 'perfect' with a surface temperature efficiency of unity. Thus, the thermal boundary condition for the gas side flow is of the 'constant wall temperature' kind.

Especially in cases of large temperature differences between the fluid and the surface, the effect of tem-

perature dependent fluid properties on the flow is significant. However, in order not to go beyond the scope of this paper, the following assumption (*Ass. 2*) is involved:

*Ass. 2:* Temperature differences are small enough to allow for the fluid properties, viscosity,  $\mu$ , thermal conductivity,  $k$ , specific heat capacity,  $c_p$ , and density,  $\rho$ , to be treated as constant.

The experimental data are presented in ref. [2] in terms of non-dimensional heat transfer and flow friction characteristics, i.e. in terms of the Colburn factor,  $j$ , and the friction factor,  $f$ , as functions  $g_j$  and  $g_f$  of the Reynolds number,  $Re$ :

$$j = St \cdot Pr^{2/3} = g_j(Re), \quad (1)$$

$$f = g_f(Re), \quad (2)$$

with the Prandtl number,  $Pr$ , the Reynolds number,  $Re$ , (based on the hydraulic radius,  $r_h$ , and the mass velocity,  $G$ ) and the Stanton number,  $St$ , defined by:

$$St = \frac{Nu}{Re \cdot Pr}, \quad (3)$$

where  $Nu$  denotes the Nusselt number, based on  $r_h$ :

$$Nu = \frac{h \cdot 4r_h}{k}. \quad (4)$$

In equation (4),  $k$  is the thermal conductivity of the gas and  $h$  denotes the gas side heat transfer coefficient

(due to Ass. 1) defined by:

$$h = \frac{Q}{A \cdot \Delta T_m}, \quad (5)$$

with the total heat,  $Q$ , transferred from the surface with area  $A$  and the log-mean temperature difference,  $\Delta T_m$ , defined as

$$\Delta T_m = \frac{\Delta T_{w-bi} - \Delta T_{w-bo}}{\ln\left(\frac{\Delta T_{w-bi}}{\Delta T_{w-bo}}\right)}. \quad (6)$$

Here,  $\Delta T_{w-bi}$  and  $\Delta T_{w-bo}$  denote the differences between the wall temperature  $T_w$  and the bulk temperatures at the inlet and the outlet of the heat transfer section,  $T_{bi}$  and  $T_{bo}$ , respectively.

The friction factor,  $f$ , (equation (2)) is defined on the basis of an equivalent shear force in flow direction, which is considered to be a combination of viscous shear, form drag and changes in momentum flux causing the pressure drop in the flow. Consequently, the friction factor  $f$  is defined by:

$$f = \Delta p_{st} \cdot \frac{2\rho}{G^2} \cdot \frac{A_c}{A}, \quad (7)$$

with the static pressure loss,  $\Delta p_{st}$ , from the inlet of the transfer surface channel to its end, the density,  $\rho$ , the mass velocity,  $G$ , the free flow cross sectional area,  $A_c$ , and the total heat transfer (or skin friction) surface area,  $A$ .

With the Colburn factor,  $j$ , given as a function of the Reynolds number only and the 2/3 power of the Prandtl number, equation (1) in combination with equation (3) involves a further assumption (Ass. 3):

*Ass. 3:* The Nusselt number,  $Nu$ , depends on the Prandtl number,  $Pr$ , to the power 1/3.

This is often used as an adequate approximation at least for gases in the laminar flow range over a moderate range of Prandtl numbers [2].

Due to the fact that  $j$  and  $f$  are expressed in terms of  $Re$  only, i.e. with no dependence on the heat exchanger flow length,  $L$ , equations (1) and (2) imply the additional assumption of:

*Ass. 4:* The  $j$  and  $f$  data represent the fully developed flow characteristics of the heat transfer surfaces with entrance effects negligible.

This assumption can be closely approached, if the test section is long enough to allow for the neglect of hydrodynamic and thermal entry effects. In the case of a heat transfer surface consisting of periodically continuing modules each showing a certain arrangement of interrupted fins, vortex generators, etc., the term 'fully developed flow' is to be understood in a macroscopic sense. Defining mean values of  $j$  and  $f$  with respect to each module of length  $l$ , (the entire surface of length  $L$  consists of  $M$  modules, with  $L = M \cdot l$ ; see Figs. A3 and A5), these mean values gradually tend towards an asymptotic limit (for

increasing  $M$ ), even though in a microscopic sense a periodic continuing development of boundary layers and subsequent dissipation characterizes each single module. In ref. [3] this situation is referred to as 'periodic fully developed flow'.

The experimental data for the Surface Types A, B, C and D [2] are presented in Figs. A1–A4 in the Appendix together with detailed diagrams of the surfaces and the governing geometry data. However, the validity of the data given in Figs. A1–A4 is not restricted to the specific scales of the test geometries [2]. Provided that geometric similarity is maintained, surfaces with different scales, e.g. hydraulic radii, are as well characterized by the given nondimensional data.

#### Numerical data

Several experimental [4, 5] and numerical investigations [6–8] of the heat transfer and the pressure loss of surfaces with different types of so called vortex generators are indicating the effectiveness of vortex generators for heat transfer augmentation in high performance heat exchangers. Despite their small scale in comparison to the overall heat transfer surface vortex generators significantly increase the heat transfer by means of an effective exchange of fluid from wall to core regions of the flow due to the induction of a strong secondary spiraling flow.

The performance data for the Type E surface (see Fig. 1 and Fig. A5 in the Appendix) have been obtained by means of a numerical prediction of the flow and temperature field in a sample geometry. The type of vortex generator, its arrangement on the heat transfer surface and the particular geometrical data have been chosen somewhat arbitrarily mainly with a view to relatively simple geometric proportions (for details see the surface diagram in Fig. A5 in the Appendix). Thus, the present type E heat transfer surface does not represent an optimum in any way. The optimization is the subject of an on-going project at the Institut für Thermo- und Fluidodynamik (ITF) [9].

The numerical scheme and its validation has already been discussed in several publications [6, 7, 10, 11], to which the reader is referred for details. Since then, substantial progress has been gained especially concerning the minimization of numerical viscosity effects and computing time [9]. Further validation work has been done and is in progress at the ITF [5, 8, 9] showing good agreement between numerical and experimental data especially concerning integral data of flow loss and heat transfer. However, the numerical data presented here are of predictive character with experiments for validation still to be carried out.

In order not to go beyond the scope of this presentation, only the main features and characteristics of the numerical scheme are summarized in the following:

The governing equations to be solved are the constant property Navier–Stokes, continuity and energy equations.

The flow simulation is restricted to the laminar range.

Both elliptical and streamwise parabolic calculations (saving of computing time) are possible.

The latter is especially convenient with respect to the special arrangement of the vortex generators on the heat transfer surface, as depicted in Fig. 2. The surface consists of  $M$  modules of length  $l$ , each with a delta wing vortex generator mounted on the surface and an 'empty' space of certain length downstream. Within each of these modules the flow and temperature field has been calculated elliptically. Interactions between the single modules are treated in a streamwise parabolic manner, i.e. upstream influences from one module to the former are neglected. Due to this treatment, the last module in a row of  $M$  modules reflects the behavior of the 'periodic fully developed flow' (consistent to the experimental performance data in the case of the Surface Types A, B, C and D), if  $M$  is sufficiently high.

As a result of the numerical prediction, Fig. 3 shows the distribution of local Nusselt numbers in the sample geometry consisting of  $M = 5$  modules for a Reynolds number,  $Re = 1000$ , and a Prandtl number,  $Pr = 0.7$ . Details concerning the flow and temperature field in the wake of a vortex generator in a channel are given in ref. [11]. The Nusselt number,  $Nu_{\overline{xy}}$ , is defined as the average of local values  $Nu_{xy}$  from both channel wall sides (one with the vortex generator (vg) mounted on and the opposite (op) without vortex generator):

$$Nu_{\overline{xy}} = \frac{1}{2} (Nu_{xy,vg-side} + Nu_{xy,op-side}), \quad (8)$$

with  $Nu_{xy}$  defined as:

$$Nu_{xy} = \frac{\left(\frac{\partial T}{\partial z}\right)_{xy,wall}}{T_{bx} - T_w} 4r_h, \quad (9)$$

where  $z$  denotes the normal direction to the surface, the index  $xy$  indicates local values at the surface coordinates  $x, y$  (see Fig. 2), the quantity  $T_{bx}$  denotes the fluid bulk temperature in the cross section at position  $x$ , and all other quantities have usual meaning as defined before. Due to the small amount of the vortex generator area to the overall surface area, the vg-surface is assumed not to influence the cross sectional mean values of  $Nu_{\overline{xy}}$ . In Fig. 3 the values  $Nu_{\overline{xy}}$  are given at three positions  $y$  of the test section, i.e. at the wing chord symmetry plane (a), at the vortex generator span position (b), and at the symmetry plane in the middle between two rows of vortex generators (c). It should be mentioned that introducing symmetric boundary conditions at positions (a) and (c) may act restrictively on the flow, suppressing possible sideward oscillations. However, symmetric boundary conditions are a convenient first guess, allowing for a considerable reduction of the computational grid size (for each single module a numerical grid with  $120 \times 40 \times 20$  grid points in  $x, y, z$ -direction has been used). Further, Fig. 3 shows the development of the cross sectional averaged Nusselt number,  $Nu_x$ , from the channel inlet downstream.  $Nu_x$  is defined to represent the integral values from the

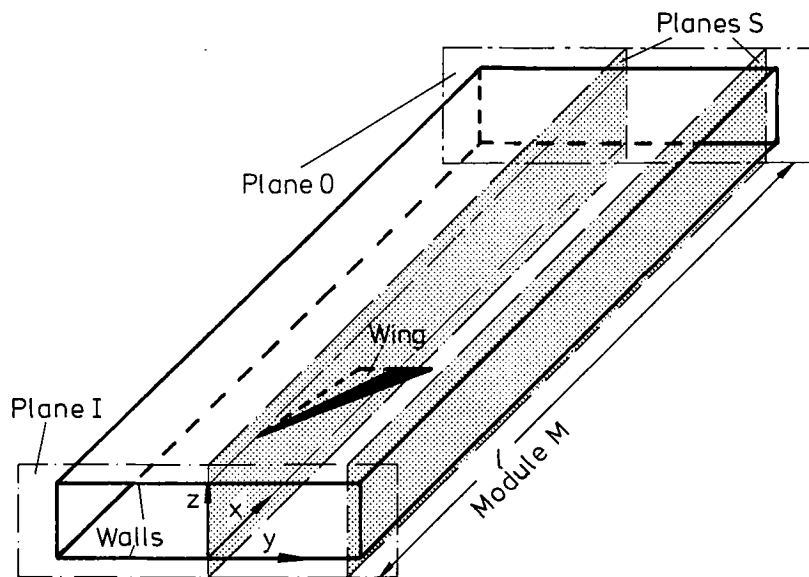


FIG. 2. Test geometry for the numerical prediction of the Surface Type E performance data. Shown is a single module  $M$  of length  $l$  with a vortex generator of delta wing type. The computational domain for elliptical computation is bounded by the module inlet (I) and outlet (O) planes, the symmetry planes (S) and the plate channel walls.

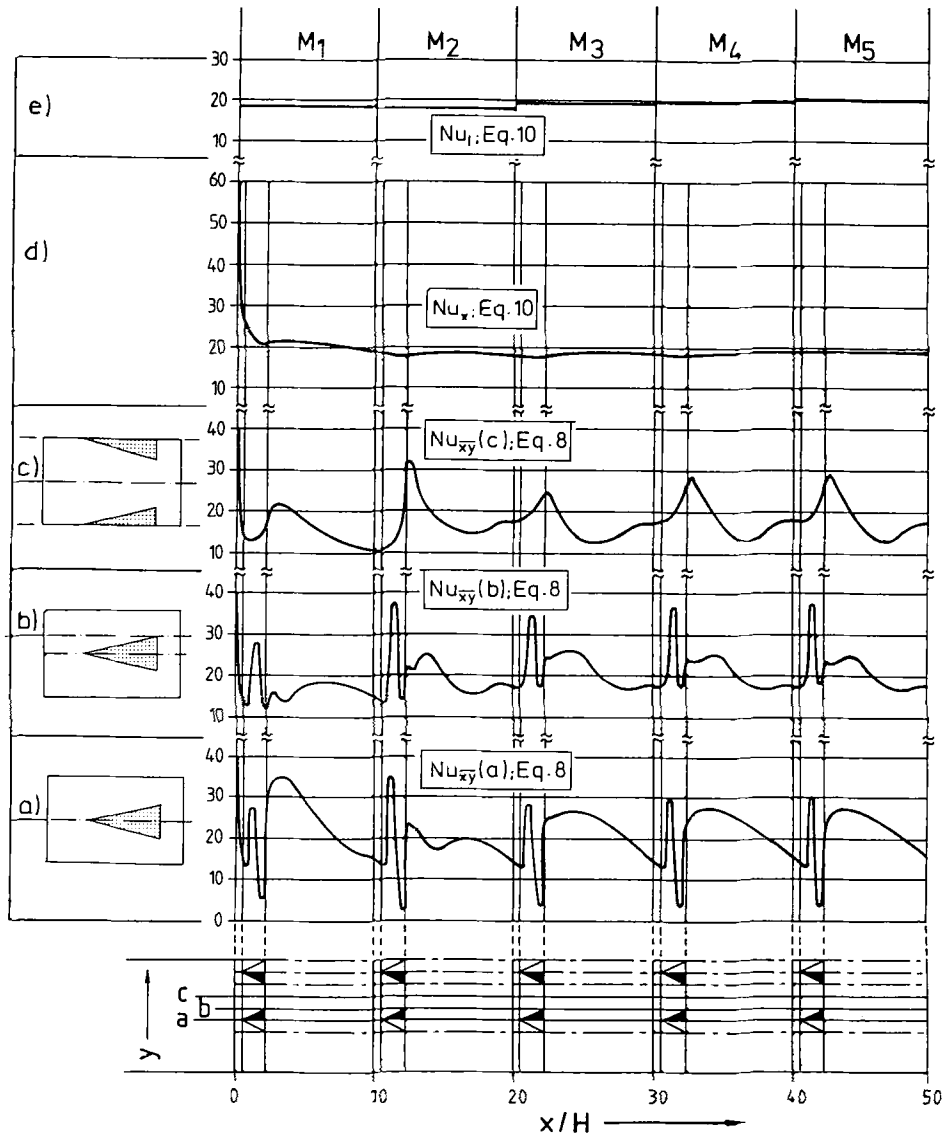


FIG. 3. Different Nusselt numbers  $Nu$  plotted versus the length coordinate  $x/H$  of the Type E surface, consisting of  $M = 5$  modules ( $Re = 1000$ ,  $Pr = 0.7$ ). Local values  $Nu_{\bar{xy}}$  (equation (8)) at three locations  $y$ : a) wing chord symmetry plane; b) wing span position; c) position between two rows. d) Development of the cross sectional mean,  $Nu_x$ , (equation (10)). e) Module averaged value,  $Nu_i$ .

inlet ( $x = 0$ ) down to an actual position  $x_a$  ( $x_a \leq L$ ):

$$Nu_x = \frac{1}{x_a} \int_{x=0}^{x=x_a} \left( \frac{1}{U_x} \int_{U_x} Nu_{xy} dU_x \right) dx, \quad (10)$$

with  $Nu_{xy}$  from equation (9) and  $U_x$  denoting the wetted perimeter of the channel at position  $x$ . Based on energy-balance considerations for a surface element  $dA$  [12], it can easily be shown, that integrating equation (10) over the entire length of the heat exchanger,  $L$ , leads to a Nusselt number,  $Nu_x$ , identical to the overall Nusselt number,  $Nu$ , defined by equations (4)–(6). Finally, the bars in Fig. 3 represent the Nusselt number average values,  $Nu_i$ , for each entire module,  $M$ , of length,  $l$ , according to equation (10) integrated from 0 to  $l$  in each module.

As can be seen from Fig. 3, the spiraling flow downstream of a vortex generator causes substantial increase in heat transfer. Due to the fixed boundary conditions at the entrance of the first module (parabolic velocity profile and uniform temperature profile) the vortex generator in the first module faces a developing basis flow in the channel.

Generally, as demonstrated by the graphs of  $Nu_{\bar{xy}}$  at the positions (a), (b), and (c) in Fig. 3, the development of the flow in a Type E geometry towards the 'periodic fully developed' asymptotic situation is governed by a superposition of two phenomena:

The first is the development of the 'global mass and energy transport flow' through the channel (e.g. development of the axial velocity profile). Starting

from the given velocity and temperature profiles at the entrance of the first module, the flow is forced to swerve to the 'nonblocked' side channels on both sides of the vortex generators. This development partially governs the flow in the first few modules. (In the wake of the vortex generator  $Nu_{\overline{xy}}$  slows down from module 1 to module 2 at position (a) while it increases at the side channel position (c).)

The second is the development of the spiraling secondary flow. Starting from the parallel flow (with no circumferential components) at the entrance of the first module, the flow is increasingly governed by strong helical vortices formed along the leading edges of the vortex generators. Further downstream, a periodic feed-in of rotating energy followed by an equivalent dissipation in each module characterizes the situation tending towards the 'periodic fully developed flow'. In this situation the counter rotating vortices cause the strongest increase in  $Nu_{\overline{xy}}$  in the downwash region at the centerline position (a) (see also ref. [11]). The downward peaks are caused by the stagnation point at the wing tip (the tip touches the opposite wall) and especially by the stagnation point at the trailing edge where the vortex generators are mounted on the wall (see  $Nu_{\overline{xy}}$  at positions (a) and (b)). The upward peaks mark positions where a superposition of the developing vortices towards the rear end of the vortex generator and peaks of the axial velocity due to the vortex generator blockage occurs.

The cross-sectional mean Nusselt number,  $Nu_x$ , starts from the high value at the entrance of module 1 and gradually tends to its asymptotic limit corresponding to the periodic fully developed values. In the case of the example given in Fig. 3 with  $Re = 1000$  and  $Pr = 0.7$ , this situation is almost already obtained at the end of the fifth module. Consequently, the corresponding module averaged Nusselt number,  $Nu_i$ , of the specific module showing asymptotic behavior has been taken as a representative value suitable for a comparison with the experimental overall data from the Surface Types A, B, C and D. The module averaged Nusselt number in this fifth module is  $Nu_i \approx 20$  (for comparison: the value for a fully developed parallel plate flow is  $Nu = 7.54$ ). A more straightforward method to obtain the periodic fully developed flow characteristics is to directly introduce periodic boundary conditions [13, 14] to the inlet and outlet planes of one single module (Fig. 2). A corresponding calculation has been carried out in order to control whether or not the fifth module showed true periodic characteristics.

Corresponding to the heat transfer data in Fig. 3, Fig. 4 shows the friction data in the sample geometry (Fig. 2).

Corresponding to the local Nusselt number distribution, Fig. 4 shows the distribution of the local surface shear stress in terms of the product of the Reynolds number,  $Re$ , and the Fanning friction factor  $c_{f,\overline{xy}}$  (averaging corresponding to equation (8)) with

$c_{f,\overline{xy}}$ , defined by:

$$c_{f,\overline{xy}} = \frac{\tau_{s,\overline{xy}}}{\rho \cdot u_m^2 / 2} = \frac{2}{Re} \cdot \frac{4r_h}{u_m} \cdot \left( \frac{\partial u}{\partial z} \right)_{xy,wall}, \quad (11)$$

with the shear stress,  $\tau_{s,\overline{xy}}$ , the mean axial velocity,  $u_m$ , the local axial velocity,  $u$ , and all other quantities with usual meaning. The high values of  $c_{f,\overline{xy}} \cdot Re$  especially at position (c) reflect the high axial velocities in the nonblocked side channels due to the blockage caused by the vortex generators. Figure 4(d) shows the development of the product  $f \cdot Re$ , with the friction factor  $f$  defined by equation (7). Figure 4(e) shows the module averaged values of the product  $f \cdot Re$  with the static pressure loss,  $\Delta p_{st}$ , denoting the pressure loss of each single entire module of length  $l$ .

The similar behavior to the corresponding values of the Nusselt number indicates the—although restricted—analogy between heat and momentum transfer. Again, the periodic fully developed situation, indicated by values  $f \cdot Re$  gradually tending to an asymptotic limit, is nearly obtained at the end of the fifth module. The module averaged value of  $f \cdot Re$  in this fifth module is  $f \cdot Re \approx 93$  (for comparison: the value for a fully developed parallel plate flow is  $f \cdot Re = 24$ ).

Numerical predictions for the Type E flow and temperature fields, as presented in Figs. 3 and 4 for  $Re = 1000$  and  $Pr = 0.7$  have been carried out for different Reynolds numbers in the range between  $500 \leq Re \leq 3000$ . In each case, the number of modules  $M$  has been chosen sufficiently high (depending on the Reynolds number) to gain Nusselt numbers and friction factors representing the asymptotic limit of the periodic fully developed flow. Furthermore, a direct periodic calculation has been carried out to control the periodic characteristic of the last module. The data are given in terms of the Colburn factor,  $j$ , and the friction factor,  $f$ , vs the Reynolds number,  $Re$ , in Fig. 5. (For completeness see also Fig. A5 (Appendix) with a detailed diagram of the Type E surface and the governing geometry data.) The comparative assessment is based on these data.

A comparison of the surface performance data given in Figs. A1–A5 (Appendix) shows values of  $j$  and  $f$  significantly higher for Types C, D and E than for A and B. Consequently, a higher heat transfer capability and, in turn, higher flow losses are involved with these types.

## PERFORMANCE DATA CORRELATIONS

The quantitative comparison of the different surfaces is based on specific performance calculation equations. It is therefore convenient to derive arithmetic expressions of the characteristics of  $j$  and  $f$  vs  $Re$  to enter the performance equations. As a satisfactory first guess [1], the  $j$  and  $f$  data from Figs. A1–A5 are uniformly correlated in consistency to equations 1 and 2 and the related assumptions (Ass.

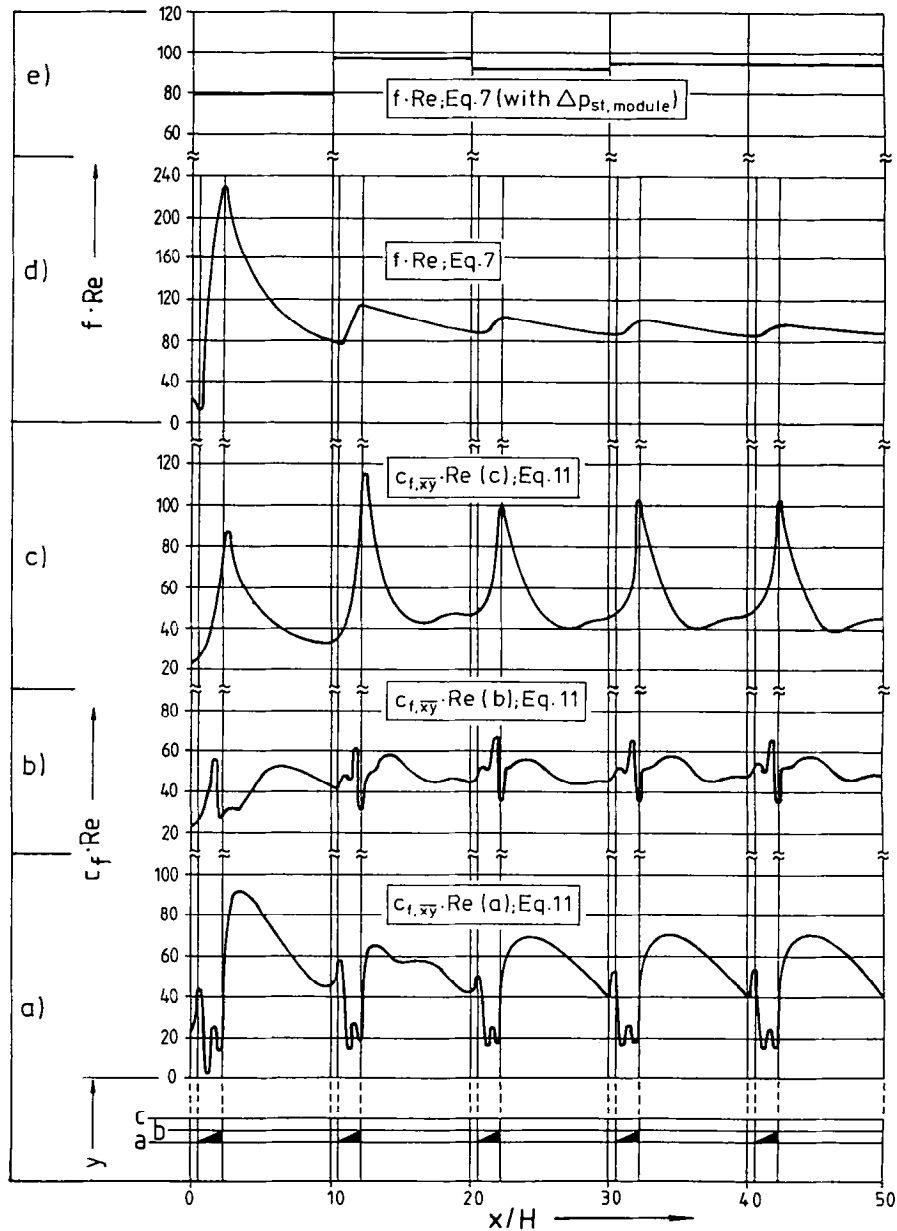


FIG. 4. Local shear stress and friction factors plotted against the length coordinate  $x/H$  of the Type E surface, consisting of  $M = 5$  modules ( $Re = 1000$ ,  $Pr = 0.7$ ). a, b, c) Local shear stress in terms of  $c_f \cdot Re$  (equation (11)) at three locations  $y$  consistent with Fig. 3. d) Development of the cross sectional mean friction factor in terms of the product  $f \cdot Re$  (equation (7)). e) Module averaged values of  $f \cdot Re$ .

3 and 4) by approaching:

$$j = a \cdot Re^m, \quad (12)$$

$$f = b \cdot Re^n, \quad (13)$$

with the coefficients and exponents  $a$ ,  $b$ ,  $m$  and  $n$  given in Table I.

In the range between  $500 \leq Re \leq 2000$ , the correlations predict the  $j$  and  $f$  data within  $\pm 6\%$  (for Type E within  $\pm 2\%$ ). Considering the spread of the experimental data this should be a satisfactory

approximation to enter the following performance comparison.

#### METHOD OF COMPARISON AND RESULTS

Aiming at reduced capital costs as a subject of optimization for heat exchanger surface design, the reduction of total heat transfer surface area is one possible resulting performance objective. Several methods for comparison [1, 15–17] often referred to



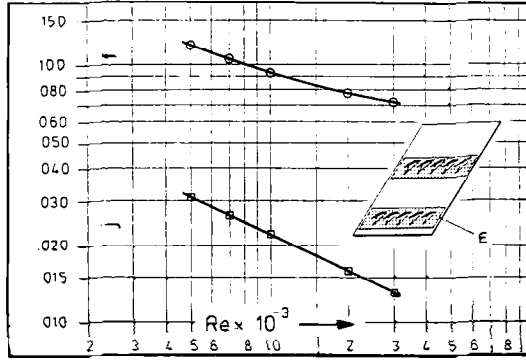
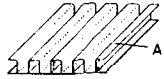

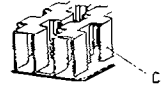
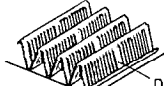
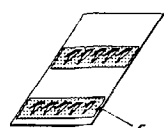


FIG. 5. Surface performance data  $j$  and  $f$  vs  $Re$  for the Type E surface based on a numerical prediction of the 'periodic fully developed' flow and temperature field. For details of the geometry see Fig. A5.

as so called Performance Evaluation Criteria (PEC) which define the performance benefits of an enhanced surface relative to a reference surface [1, 17] have been proposed. A PEC is established by selecting one of the operational variables for the performance objective, subject to design constraints on the remaining variables. For the comparative assessment of the surfaces A, B, C, D and E the so called VG-1 criterion [1] is used seeking for reduced total transfer area,  $A$ , while meeting the constraints of fixed pumping power,  $P$ ,

Table 1. Coefficients and exponents  $a$ ,  $b$ ,  $m$  and  $n$  in equations (12) and (13), correlating the data  $j$  and  $f$  as a function of  $Re$  for the Surface Types A, B, C, D and E within  $\pm 6\%$  in the range  $500 \leq Re \leq 2000$

Surface Types	Coefficients, Exponents			
	$j = a \cdot Re^m$		$f = b \cdot Re^n$	
	$a$	$m$	$b$	$n$
	1.422	-0.791	7.183	-0.850
	0.720	-0.716	5.022	-0.793
	0.230	-0.387	5.002	-0.588
	0.150	-0.351	1.333	-0.432
	0.634	-0.484	0.906	-0.323

fixed heat duty,  $Q$ , and fixed mass flow rate,  $W$ :

$$\frac{Q}{Q_o} = \frac{P}{P_o} = \frac{W}{W_o} = 1. \quad (14)$$

The index o indicates an appropriate reference surface. The choice of the reference surface has no effect on the comparative assessment of the surfaces under consideration. Thus, the Surface Type A has been chosen to act as reference surface so that the remaining Types B, C, D and E are assessed with respect to Type A. As a geometrical constraint, the hydraulic radius,  $r_h$ , is fixed. Although not necessary concerning the following derivations (equations (16)–(26)), this constraint is appropriate in order to expel the influence of  $r_h$  on the parameters of concern and thus on the comparison of the different surface types. The experimental data of concern [2] have been derived from geometries with slightly different hydraulic radii (the numerical results are dimensionless, see Fig. A5). Nevertheless, the resulting basic performance data (given in Figs. A1–A4 and equations (12) and (13) are independent from  $r_h$ , i.e.

$$\frac{r_h}{r_{ho}} = 1, \quad (15)$$

means a comparison of slightly up- or downscaled versions of those test geometries subject to the measurements in ref. [2]. The pumping power,  $P$ , is related to the pressure drop,  $\Delta p_{st}$ , by:

$$P = W \cdot \frac{\Delta p_{st}}{\rho} = G \cdot A_c \cdot \frac{\Delta p_{st}}{\rho}. \quad (16)$$

Substituting for  $\Delta p_{st}$  from equation (7), involving the constraint of fixed hydraulic radius,  $r_h$ , (equation (15)) and assuming constant properties (Ass. 2), the pumping power ratio  $P/P_o$  of a given surface relative to the reference surface (index o) can be derived from equation (16) in terms of the friction factor,  $f$ , the Reynolds number,  $Re$ , and the total surface area,  $A$ :

$$\frac{P}{P_o} = \frac{f}{f_o} \cdot \left( \frac{Re}{Re_o} \right)^3 \cdot \frac{A}{A_o}. \quad (17)$$

The heat flow rate,  $Q$ , is given by:

$$Q = \varepsilon \cdot c_p \cdot W \cdot \Delta T_{i-w}, \quad (18)$$

with the thermal effectiveness,  $\varepsilon$ , as in common use [12] (in general depending on the flow arrangement, counter flow, cross flow, etc.), the flow-stream capacity rate,  $c_p \cdot W$ , and the difference between fluid inlet temperature,  $T_i$ , and the constant wall temperature,  $T_w$ , (assumption Ass. 1). Another constraint involved with the VG-1 criterion is a fixed  $\Delta T_{i-w}$ :

$$\frac{\Delta T_{i-w}}{\Delta T_{i-w,o}} = 1. \quad (19)$$

Accounting for equations (14), (18) and (19), and the governing assumptions (Ass. 1 and 2) the relative

heat flow rate,  $Q/Q_o$ , is given by:

$$\frac{Q}{Q_o} = \frac{\varepsilon}{\varepsilon_o} = 1. \quad (20)$$

Since the operating conditions for the surfaces under comparison are identical,  $\varepsilon$  and  $\varepsilon_o$  are governed by the same function  $g(NTU)$ , with  $NTU$  denoting the Number of Thermal Transfer Units (e.g.  $\varepsilon = 1 - \exp(-NTU)$  for evaporators or condensers with  $T_w = \text{const}$ ):

$$\frac{\varepsilon}{\varepsilon_o} = \frac{g(NTU)}{g(NTU_o)}, \quad (21)$$

with  $NTU$  related to the Colburn factor,  $j$ , by:

$$NTU = h \cdot \frac{A}{c_p \cdot W} = j \cdot Re \cdot Pr^{1/3} \cdot \frac{k}{4r_h} \cdot \frac{A}{c_p \cdot W}. \quad (22)$$

Involving the constraint of fixed mass flow rate,  $W$ , (equation (14)) and hydraulic radius,  $r_h$ , (equation (15)) and assuming constant properties (Ass. 2), equation (21) leads to the following expression meeting the constraint of fixed heat duty (equation (20)):

$$\frac{NTU}{NTU_o} = \frac{j}{j_o} \cdot \frac{A}{A_o} \cdot \frac{Re}{Re_o} = 1. \quad (23)$$

By eliminating  $A/A_o$  from equations (17) and (23), one obtains

$$\frac{Re}{Re_o} = \left( \frac{j}{j_o} \cdot \frac{f_o}{f} \right)^{1/2}. \quad (24)$$

Thus, with  $j$ ,  $j_o$ ,  $f$  and  $f_o$  from equations (12) and (13) respectively, the operational Reynolds number,  $Re$ , can be determined explicitly in dependence on a specified reference Reynolds number,  $Re_o$  (keeping in mind that the right side of equation (24) is a function of both  $Re$  and  $Re_o$ ). Once  $Re$  and  $Re_o$  are known, the area ratio  $A/A_o$  can be obtained by rewriting equation (23):

$$\frac{A}{A_o} = \frac{j_o}{j} \cdot \frac{Re_o}{Re}. \quad (25)$$

The free flow area ratio  $A_c/A_{c,o}$  is governed by the constraint of fixed mass flow rate,  $W$ . Involving the relation  $W = G \cdot A_c$  and substituting for  $G$  from the definition of the Reynolds number (with  $r_h$  fixed) one obtains:

$$\frac{A_c}{A_{c,o}} = \frac{Re_o}{Re}. \quad (26)$$

To give an example, assume that the reference Surface Type A operates at  $Re_o \equiv Re_A = 1000$ . Inserting the Type E surface performance data, equation (24) yields  $Re_E = 887$ . The total transfer surface area ratio is obtained from equation (25) to  $A_E/A_A = 0.286$ . So the Type E surface requires only about 30% the surface area to provide the same heat flow rate,  $Q$ , and pumping power,  $P$ , as the Type A surface, with a slight increase in free flow area of about 13% (equation (26)).

The comparative assessment of the surfaces under

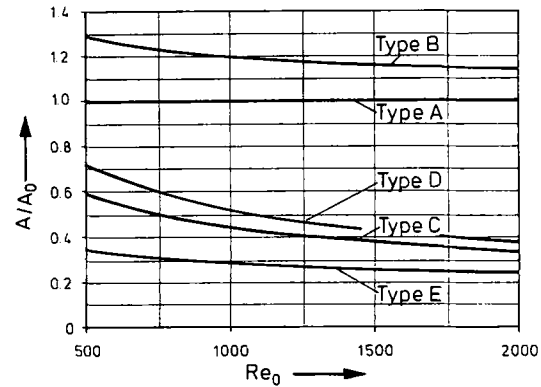


FIG. 6. Total heat transfer area ratio  $A/A_o$  plotted against the reference surface operational Reynolds number  $Re_o$  for  $Q/Q_o = 1$ ,  $P/P_o = 1$ ,  $W/W_o = 1$ ,  $\Delta T_{i-w}/\Delta T_{i-w,o} = 1$ , and  $r_h/r_{h,o} = 1$ . Given are the results for the Surface Types B, C, D and E with respect to the reference Surface Type A.

consideration has been carried out by employing this method. The results are given in Fig. 6 for a range of reference Reynolds numbers  $500 \leq Re_o \leq 2000$ .

It is evident from Fig. 6 that the Type E vortex generator surface provides the largest saving in heat exchanger surface area and thus in heat exchanger volume. It is followed by the Type C offset strip fin and the Type D louvered fin surfaces, surfaces already in widespread common use. The least effective surface type with regard to the surface area needed is the Type B surface, a fact that has already been documented from several authors applying different performance assessment methods (see page 198 in ref. [15]).

## CONCLUSION

Despite the uncertainties involved with the comparative assessment presented here—namely uncertainties in the experimental and numerical basic performance data and their interpretation (Ass. 1–4) and uncertainties due to the algebraic correlation of these data (equations (12) and (13))—the vortex generator surface design seems to be a relatively innovative design with a high performance potential. Thus, optimization of the heat transfer surfaces with vortex generators seems to be worthwhile in order to fully appreciate their performance potential. For this optimization the following has to be varied: vortex generator shape (rectangular, delta, etc.), size, angle of attack, aspect ratio as well as their arrangement on the primary surface (mounted on, stamped out, in row, staggered, etc.). Furthermore, it has been shown that numerical computations with the full Navier–Stokes equations can be used for parametric studies of complex heat transfer surfaces.

## REFERENCES

1. R. L. Webb, Enhancement of single phase heat transfer. In *Handbook of Single Phase Convective Heat Transfer* (Edited by S. Kakac, R. K. Shah and A. E. Bergles), pp. 17-1-62. Wiley, New York (1987).
2. W. M. Kays and A. L. London, *Compact Heat Exchangers* (3rd Edn). McGraw-Hill, London (1984).

3. S. V. Patankar and K. M. Kelkar, Numerical prediction of fluid flow and heat transfer in a circular tube with longitudinal fins interrupted in the streamwise direction, *J. Heat Transfer* **112**, 342–348 (1990).
4. M. Fiebig, P. Kallweit and N. K. Mitra, Wing type vortex generators for heat transfer enhancement. In *Proc. 8th Int. Heat Transfer Conf.*, vol. 5, pp. 2906–2916. San Francisco (1986).
5. S. Tiggelbeck, Experimentelle Untersuchungen an Kanalströmungen mit Einzel- und Doppel-Wirbelzeugerreißen für den Einsatz in kompakten Wärmetauschern, Ph.D. Thesis, Ruhr University of Bochum, FRG (1990).
6. U. Brockmeier, M. Fiebig and N. K. Mitra, Multigrid Marcer and Cell (SOLA) Algorithm for Three-Dimensional Flow Computations. In *Proc. 6th Gamm Conf. on Numerical Fluid Dynamics*, Vol. 13, pp. 23–30. FRG (1986).
7. M. Fiebig, U. Brockmeier, N. K. Mitra and Th. Guentermann, Structure of velocity and temperature fields in laminar channel flows with longitudinal vortex generators, *Numerical Heat Transfer, Part A* **15**, 281–302 (1989).
8. Th. Guentermann, M. Fiebig and N. K. Mitra, Heat transfer enhancement in heat exchangers by longitudinal vortex generators. In *Proc. of the ASME Annual Meeting* (Edited by D. L. Rhode and J. Tuzson), Vol. 101, pp. 83–90, Nov. 25–30. Texas (1990).
9. Th. Guentermann, Dreidimensionale stationäre und selbsteregt-schwingende Strömungs- und Temperaturfelder in Hochleistungs-Wärmeüberträgern mit Wirbelzeugern, Ph.D. Thesis, Ruhr University of Bochum, FRG (1992).
10. C. W. Hirt, B. D. Nichols and N. C. Romero, SOLA—A numerical solution algorithm for transient fluid flows, Tech Rep. LA-5652, Los Alamos Scientific Laboratory, Los Alamos, N.M. (1975).
11. U. Brockmeier, M. Fiebig, N. K. Mitra and Th. Guentermann, Heat transfer enhancement in fin-plate heat exchangers by wing type vortex generators, *Chem. Eng. Technol.* **12**, 288–294 (1989).
12. R. K. Shah, Basic design methods. In *Low Reynolds Number Flow Heat Exchangers* (Edited by S. Kakac, R. K. Shah and A. E. Bergles), pp. 21–74. Hemisphere, Washington D.C. (1983).
13. S. V. Patankar, C. H. Liu and E. M. Sparrow, Fully developed flow and heat transfer in ducts having streamwise—periodic variations of cross-sectional area, *J. Heat Transfer* **99**, 180–186 (1977).
14. K. M. Kelkar and S. V. Patankar, Numerical prediction of flow and heat transfer in a parallel plate channel with staggered fins, *J. Heat Transfer* **109**, 25–30 (1987).
15. R. K. Shah, Compact heat exchanger surface selection methods. In *Proc. 6th Int. Heat Transfer Conf.*, Vol. 24, pp. 193–199 (1978).
16. T. A. Cowell, A general method for comparison of compact heat transfer surfaces, *J. Heat Transfer* **112**, 288–294 (1990).
17. R. L. Webb, Performance evaluation criteria for use of enhanced heat transfer surfaces in heat exchanger design, *Int. J. Heat Mass Transfer* **24**, 715–726 (1981).

#### APPENDIX

The comparative assessment is based on the heat exchanger performance data  $j$  and  $f$  versus Reynolds number,  $Re$ . In case of the Surface Types A, B, C and D, these data have been taken from experimental results published in ref. [2]. In the case of the Surface Type E, the data are results of a numerical prediction of the flow and temperature field in the sample geometry.

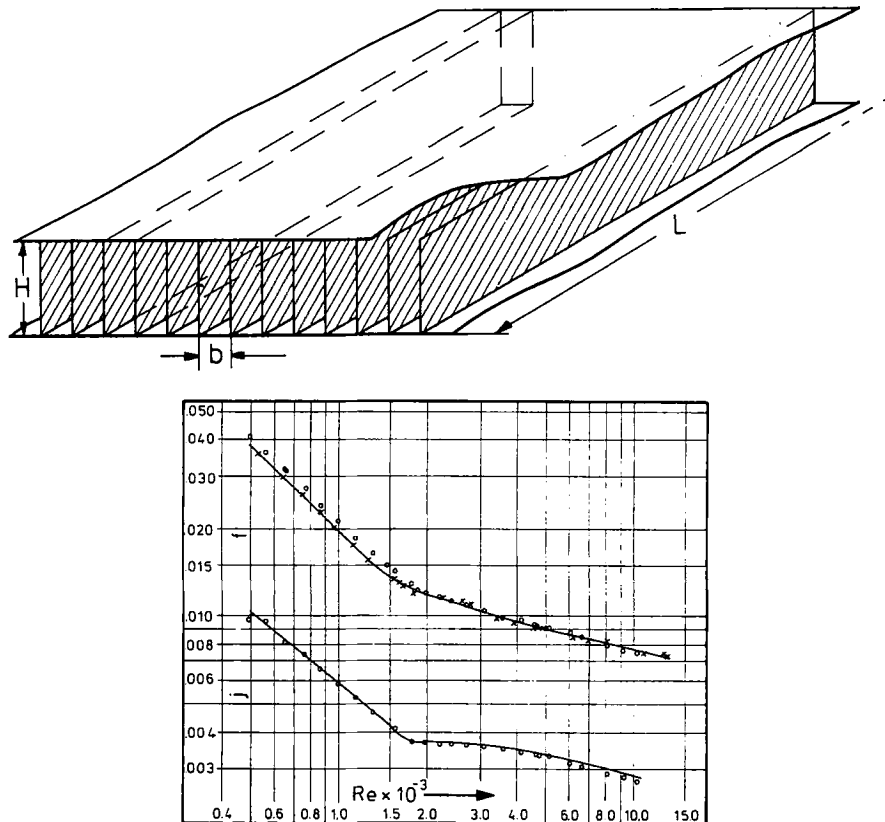


FIG. A1. Performance data  $j$  and  $f$  vs Reynolds number,  $Re$ , for the Surface Type A. The surface is a parallel plate channel geometry with rectangular fins (performance and geometry data are published in ref. [2] under log number 11.11(a)). Geometrical data:  $b/H = 0.19$ ,  $L/H = 16.68$ ,  $r_n = 0.880 \times 10^{-3}$  m.

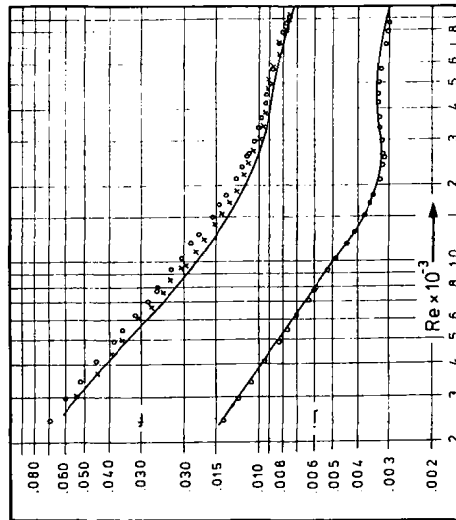
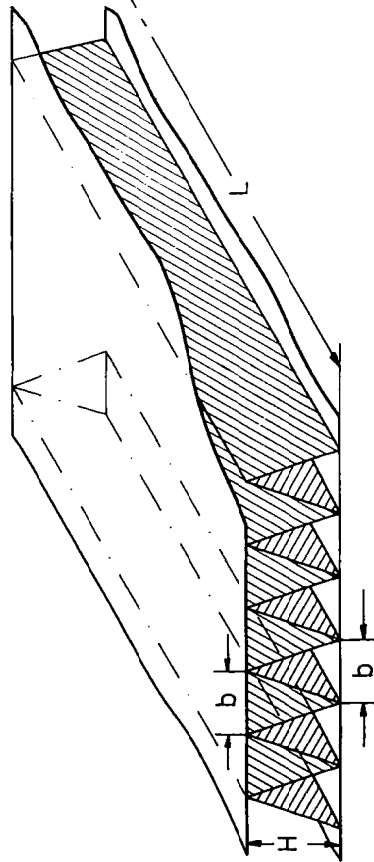


FIG. A2. Performance data  $j$  and  $f$  vs Reynolds number,  $Re$ , for the Surface Type B. The surface is a parallel plate channel geometry with triangular fins (performance and geometry data are published in ref. [2] under the log number 11.94 T). Geometrical data:  $b/H = 0.67$ ,  $L/H = 20.08$ ,  $r_h = 0.718 \times 10^{-3}$  m

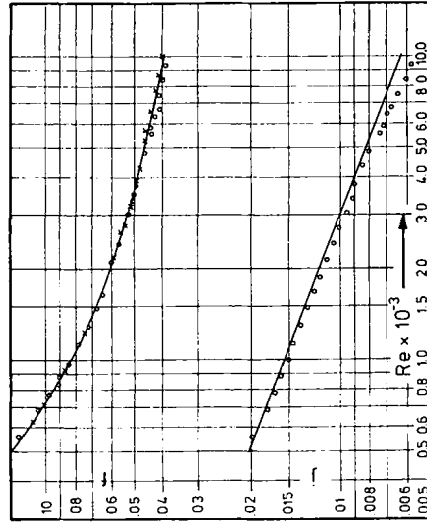
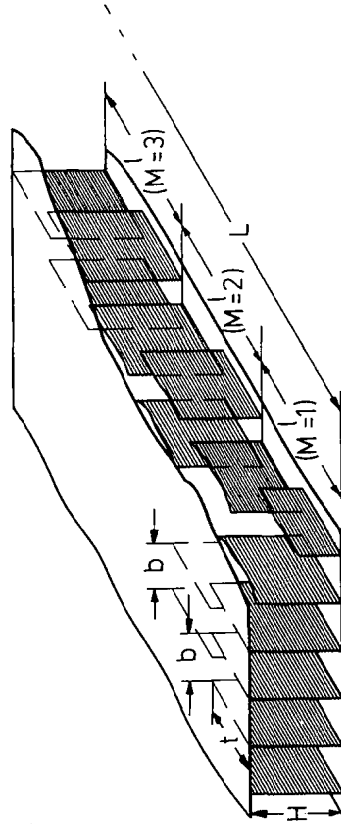


FIG. A3. Performance data  $j$  and  $f$  vs Reynolds number,  $Re$ , for the Surface Type C. The surface is a parallel plate channel geometry with offset strip fins (performance and geometry data are published in ref. [2] under the log number 3/32-12.22). Geometrical data:  $h/H = 0.17$ ,  $t/H = 0.19$ ,  $l/H = 0.38$ , fins staggered symmetrically,  $r_h = 0.853 \times 10^{-3}$  m and  $L = M \cdot l$  with  $M =$  number of modules.

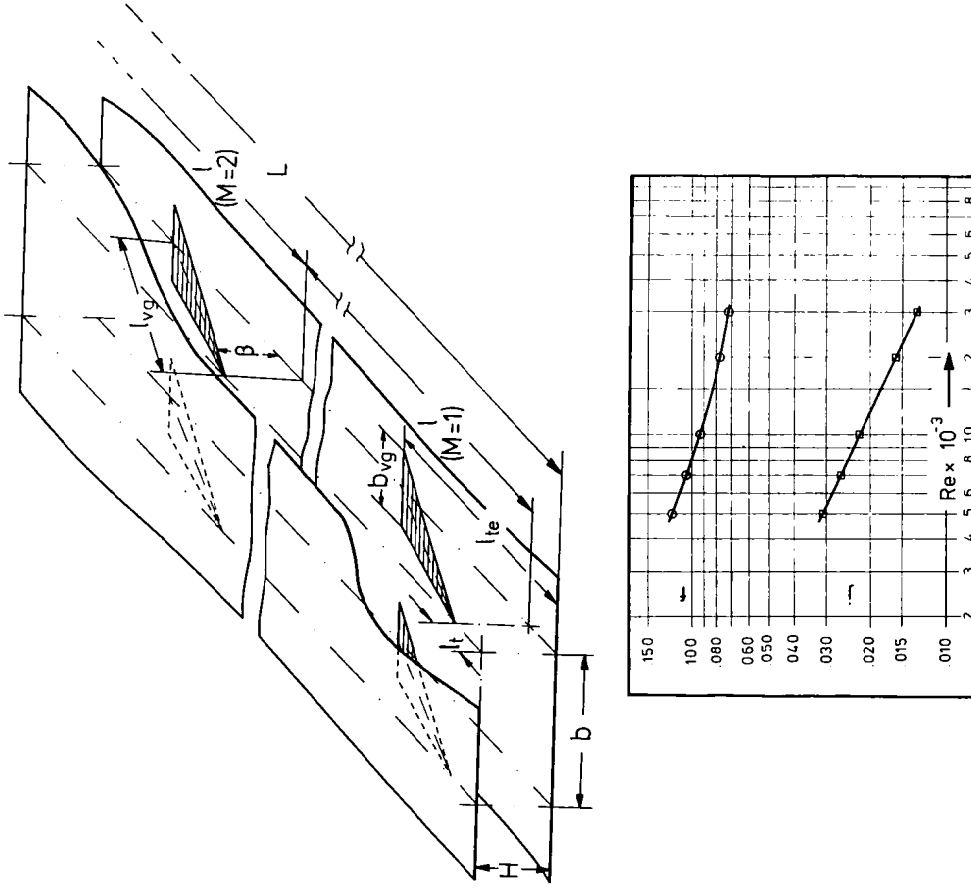


FIG. A5. Performance data  $j$  and  $f$  vs Reynolds number,  $Re$ , for the Surface Type E. The surface is a parallel plate channel geometry with vortex generators mounted on one channel plate. The performance data are a result of a numerical prediction. Geometrical data:  $b/H = 2$ ,  $l/H = 10$ ,  $l_t/H = 0.5$  (index  $t = \text{vg-tip}$ ) and  $l_{te}/H = 2.23$  (index  $te = \text{vg-trailing edge}$ ),  $l_{vg}/H = 2$  (index  $vg = \text{vortex generator}$ ),  $b_{vg}/H = 1$ ,  $\beta = 30^\circ$ ,  $r_h = 0.48H$  ( $= 0.5H$  for parallel plate channel without  $vg$ ),  $L = M \cdot l$  with  $M = \text{number of modules}$ .

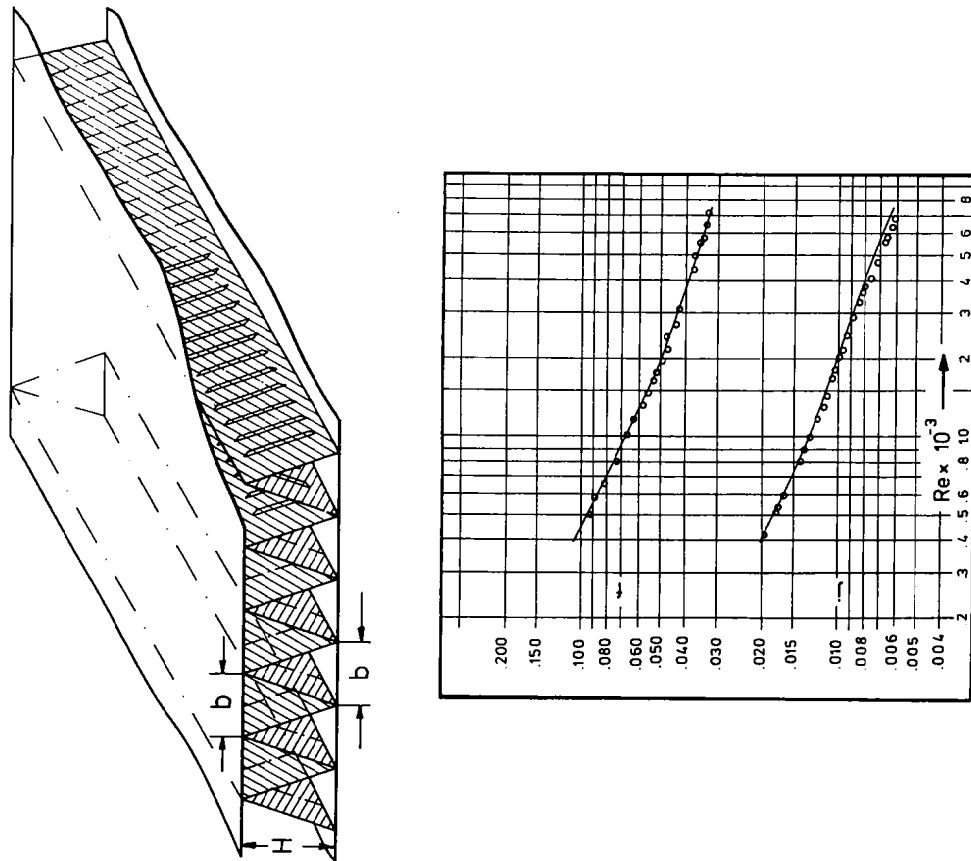


FIG. A4. Performance data  $j$  and  $f$  vs Reynolds number,  $Re$ , for the Surface Type D. The surface is a parallel plate channel geometry with louvers fins (performance and geometry data are published in ref. [2] under log number 3/16-11.1). Geometrical data:  $b/H = 0.72$ ,  $r_h = 0.771 \times 10^{-3}$  m. For geometrical details concerning the louvers see ref. [2, page 237]